Available online at www.sciencedirect.com
ScienceDirect
Energy Reports 8 (2022) 247–258
www.elsevier.com/locate/egyr

2022 The 5th International Conference on Renewable Energy and Environment Engineering (REEE 2022), 24–26 August, 2022, Brest, France

Dynamic power decoupling for low-voltage ride-through of grid-forming inverters

Feng Ji[a,*], Zhuang Xu[b,*], C. Gerada[b]

[a] Faculty of Science and Engineering, University of Nottingham Ningbo China, Ningbo 315100, China
[b] Zhejiang Aviation Electrification Technology Engineering Research Center, University of Nottingham Ningbo China, Ningbo 315100, China

Received 3 October 2022; accepted 6 October 2022
Available online 20 October 2022

Abstract

In grid-forming technologies, the power controllers emulate the operation of synchronous generator. The frequency regulation, power-decoupling and virtual inertia are mostly achieved on the basis of small-signal models. However, the transient power and coupling mechanism of the converters have not been revealed thoroughly. If the voltage of grid-connection point drops because of power grid failure, it may lead to unbalance and instability for virtual synchronous generator (VSG). Normally, the active power is required to decrease to restrain the current and the reactive power is required to increase to support the voltage of the power grid during the fault. Therefore, the dynamic power decoupling is sensitive for the low-voltage ride-through (LVRT) for VSG. The traditional power decoupling control based on small signal models is not perfect for LVRT. In this paper, a graphical model is proposed for the analysis of transient power transfer and the reflection of the impact caused by the remarkable changes of the power angle and the grid voltage. The voltage compensation is designed to remedy the effect of power angle disturbance. The dynamic performance for LVRT can be improved by the control strategy based on large signals. The simulation and experiment results show that the suggested method is feasible.

Peer-review under responsibility of the scientific committee of the 5th International Conference on Renewable Energy and Environment Engineering, REEE, 2022.

Keywords: Voltage-source converters; Virtual synchronous generator; Transient power; Graphical model

1. Introduction

Voltage-source converters (VSC) have been extensively used as interfaces between power grids and renewable energy generations. Generally, depending on the suitability of various applications, there are two ways of controlling the VSCs [1–3]: grid-following or grid-forming. In the grid-following mode, VSC behaves as a controllable current source under a vector current control *scheme* [2,3]. The synchronization with power grids is realized by means of Phase-Locked Loops (PLLs). In the case that the grid connection is weak, the stability or synchronization may be

* Corresponding authors.
E-mail addresses: Feng.Ji@nottingham.edu.cn (F. Ji), John.Xu@nottingham.edu.cn (Z. Xu).

https://doi.org/10.1016/j.egyr.2022.10.083

Peer-review under responsibility of the scientific committee of the 5th International Conference on Renewable Energy and Environment Engineering, REEE, 2022.

lost due to the disturbance or malfunction of PLLs. Instead, the grid-forming actively establishes the voltage and frequency and provides regulations.

In the off-grid operating mode, the frequency of self-supply power systems is very sensitive to the variation of working loads. The frequency fluctuation will affect the safe and stable operation of the whole system. Therefore, one of the key control strategies is how to maintain the stability with regards to the frequency and voltage for the self-supply power system. Because synchronous generator has the moment of inertia and damping coefficient, it is friendly to the power grid. The method of excitation and frequency control of VSG [4,5] can be applied. The characteristics of the synchronous generators can be emulated by the power controllers. The schematic diagram of traditional VSG is shown in Fig. 1.

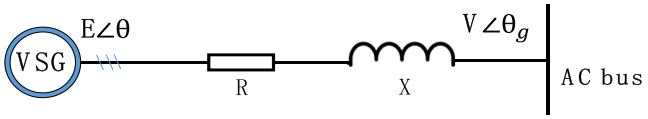

Fig. 1. Equivalent circuit of a VSG tied to an AC bus.

Currently, the grid-forming control still has stability issues under different conditions. Most analysis has been accomplished based on small-signal models and linear control theories. Remarkable changes of the power angle and grid voltage may not be reflected sufficiently and accurately on the modeling. The stable equilibrium points indicated by the linearization may not exist under certain disturbances. Considering the non-linearity aspect of the control scheme, the transient power transfer can be analyzed by establishing nonlinear differential equations. Nevertheless, it is challenging to solve the equations and reveal the physical insights in the time domain. A non-linear technique termed as the equal area criterion (EAC) [2] has been utilized to analyze stability of the VSCs with large-signal perturbations. the transient behavior of the VSCs is described by using a reduced order nonlinear model. Whereas, there is still a research gap between the power dynamics and stability constraints due to the deficiency of effective analytical methods.

The inverters based on VSG perform like voltage sources. It will output excessive current when the power grid voltage sags because of power grid failure. The VSG is not allowed to disconnected from the power grid immediately according to the grid codes. At the same time, the extra reactive power is required to support the voltage of the power grid. The deeper the power grid voltage sags, the greater the reactive power required to be supplied for the power grid under LVRT control [6–8]. In [9], a power decoupling method is proposed for photovoltaic converters under LVRT control. The operation mode can be switched between LVRT mode and maximum power point tracking mode. But the scheme is only designed to be based on one-phase photovoltaic inverters. In [10], a control method to improve the transient stability of VSG has been described in detail. It can weaken the oscillation when VSG is in the short-circuit fault. It can fulfill the requirement of LVRT while improving the transient stability. But the transient power transfer and decoupling is not described thoroughly in the paper.

The major contribution of this paper is the proposal of a graphical model in Section 3 that presents transient power transfer on a $P-Q$ reference frame. The upper and lower limitations of the power dynamics are derived from the model. The maximum power angle is also reflected in the power circle considering the voltage constraints of the VSC and the grid. A linear control method is adopted to maintain the power stabilities by incorporating the control parameters with non-linear characteristics.

Compared with the traditional power decoupling method, the proposed control scheme can weaken greatly the link of the reactive power and power angle for large signals by voltage compensation. The graphical power decoupling can play an important role in improving the transient response of LVRT. The simulation and experimental results verify the effectiveness of the proposed schemes.

2. Analysis of the relationship between P and Q

Fig. 2 illustrates the block diagram of the overall structure of a three-phase VSC and its control schemes. In Fig. 2, a grid-forming VSC converts the renewable energy into the form of energy that complies with the power grid. A filter built with inductors and capacitors and the line impedance are located between the VSC and the point of common-coupling (PCC). The active-power P control and reactive-power Q control loops (Fig. 3) provide regulations of the

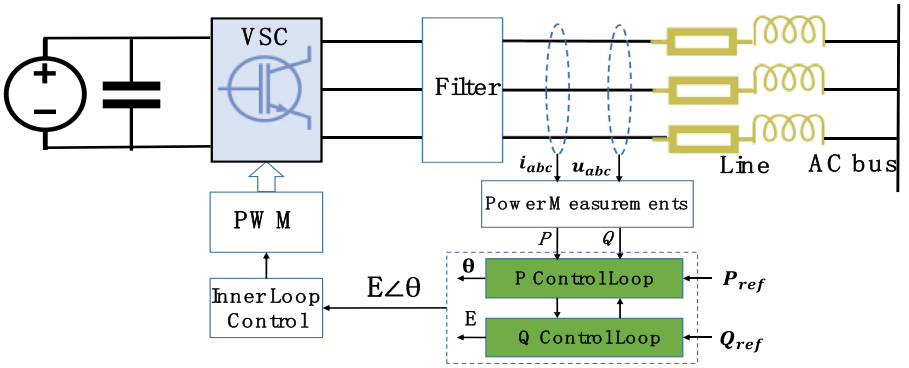

Fig. 2. Overall structure of the VSG system.

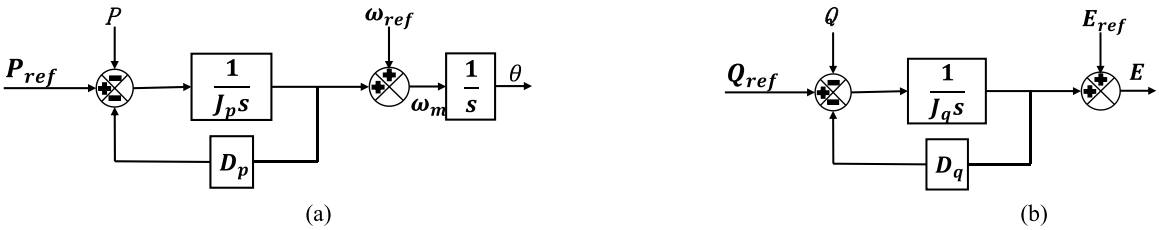

Fig. 3. (a) P control loop and (b) Q control loop.

frequency (or phase) and voltage magnitude. Various grid-forming control strategies can be implemented in these controllers. The grid frequency and output power are measured by the frequency detector and the power meter blocks, respectively.

Considering that the power angle may vary considerably during transient operations and the ratio of R to X is large in the transmission line, the output active-power P and reactive-power Q of the VSG [5] can be expressed as:

$$P = \frac{EV}{\sqrt{R^2+X^2}}\sin(\delta+\tan^{-1}\frac{R}{X}) - \frac{RV^2}{\sqrt{R^2+X^2}} \tag{1}$$

$$Q = \frac{EV}{\sqrt{R^2+X^2}}\cos(\delta+\tan^{-1}\frac{R}{X}) - \frac{XV^2}{\sqrt{R^2+X^2}} \tag{2}$$

where E and V are the VSG output voltage and AC bus voltage, respectively. δ is the phase displacement between E and V. It is observed that both P and Q exhibit nonlinear behaviors with sine and cos functions. They are coupled by the mutual influence of the δ and E. φ can be defined as:

$$\varphi = \delta + \tan^{-1}\frac{R}{X} \tag{3}$$

δ_0 and E_0 are the power angle and VSG voltage at the operating point. If $\varphi \neq 0$, then P and Q are coupled and dependent on each other.

3. Graphical power decoupling of large signals

In this Section, a graphical model is presented for the large-signal analysis of transient power transfer for grid-forming VSC.

3.1. The model

From (1) and (2), a mathematical expression involving both P and Q is derived:

$$(P+\frac{RV^2}{\sqrt{R^2+X^2}})^2+(Q+\frac{XV^2}{\sqrt{R^2+X^2}})^2=\left(\frac{EV}{\sqrt{R^2+X^2}}\right)^2 \tag{4}$$

Eq. (4) represents a power circle illustrated in Fig. 4 in the P–Q reference frame. The circle is centered at $\left[-\frac{RV^2}{\sqrt{R^2+X^2}},-\frac{XV^2}{\sqrt{R^2+X^2}}\right]$. The radius is $\frac{EV}{\sqrt{R^2+X^2}}$. In general, the VSG operates in the first quadrant. P_{max} is the maximum active power point where δ reaches the upper limit with the regulation of E. Q_{max} is the maximum reactive power at the voltage levels of E and V. It can be demonstrated that the existence of the line resistance reduces P_{max}.

The point S in Fig. 4 represents an arbitrary operating point that moves on the circle provided that both $|E|$ and $|V|$ are fixed. The motion of A indicates a variation of P–Q. For instance, the increment of δ in the tangential direction leads to a change of P. The movement in the axial direction will result in the variation of both E and Q.

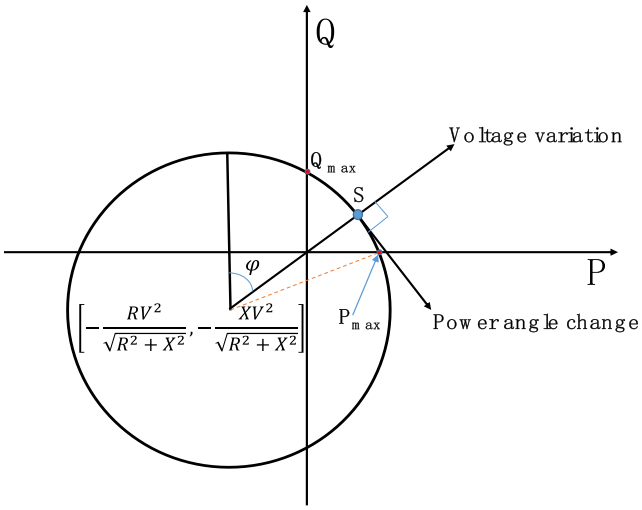

Fig. 4. A graphical presentation of the coupling of P and Q on the P–Q reference frame.

3.2. Power coupling of P and Q

The small-signal model is unable to describe the dynamic power trajectory and reflect the impact caused by the remarkable change of δ and E. To exploit the power coupling on the basis of the graphical model in Fig. 5, it is assumed that the initial working point is at A with the coordinate (P_1, Q_1). Then, in response to the reference step-down of P, the P control-loop will reduce the power angle to generate less active power. The angle change is denoted as $\Delta\delta$. This perturbation also drives Q to change. The Q control-loop will see the variation ΔQ and calculate a new Q_{ref}. By using a linear controller such as droop control or PI control etc., the capability of dynamic regulating is limited. Q will not be brought back to its normal value rapidly. In worst case, the working point moves along or in the junction of the circle from the position A to B if less Q control action is taken. The power coordinate at B is (P_2, Q_2). The radius of the circle is kept at $r=\frac{EV}{\sqrt{R^2+X^2}}$. In the triangle ΔOBA,

$$\frac{1}{2}AB=r\sin(\Delta\delta/2) \tag{5}$$

Hence, the active power change is:

$$\Delta P=AB\cos(\varphi_1-\Delta\delta/2) \tag{6}$$

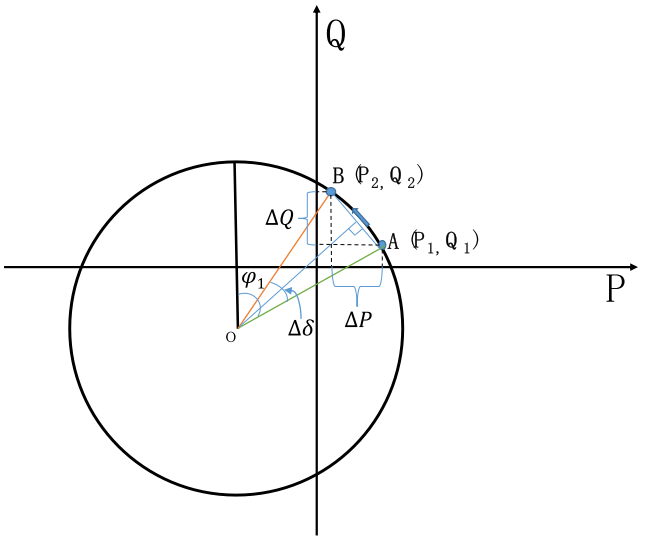

Fig. 5. The coupling of ΔP and ΔQ during a step-down operation of P.

Due to the ΔP, ΔQ is:

$$\Delta Q = \Delta P \tan(\varphi_1 - \Delta\delta/2) \tag{7}$$

Hence, the dynamic coupling between ΔP and ΔQ can be represented by the following equation:

$$\Delta Q = \Delta P \tan[\delta_1 + \tan^{-1}(R/X) - \Delta\delta/2] \tag{8}$$

where δ_1 is the power angle at the working point A. It is observed from (8) that the coupling is determined by both R/X and $\Delta\delta$. Based on the analysis above, to quantify the degree of coupling, a relative coupling factor is defined as:

$$F_c = \tan[\delta_1 + \tan^{-1}(R/X) - \Delta\delta/2] \tag{9}$$

The relationship of the F_c against R/X and $\Delta\delta$ is plotted in Fig. 6. 2-D views of the characteristics of F_c versus $\Delta\delta$ is in Fig. 7(a) where R/X varies from 0 to 0.25 and 0.6. Fig. 7(b) is a 2-D plot of F_c versus R/X where $\Delta\delta$ changes from 0 to 1.

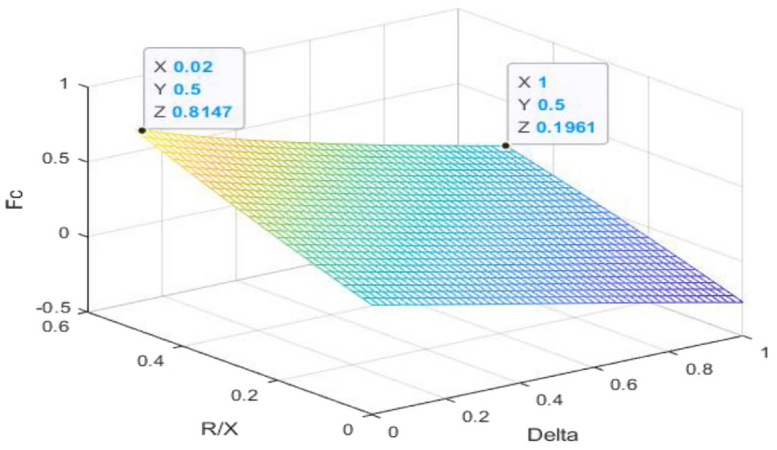

Fig. 6. Relationship of the coupling factor F_c against R/X and $\Delta\delta$.

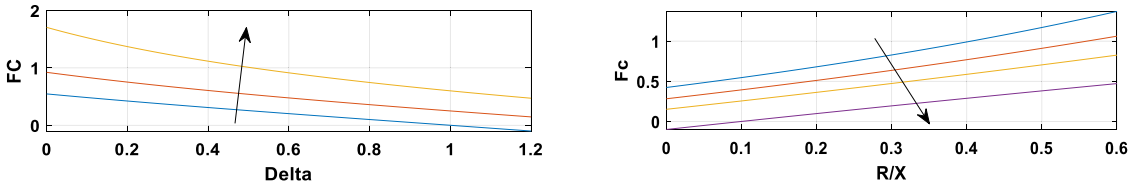

Fig. 7. (a) Characteristics of F_c versus (R/X = 0, 0.25, 0.6) and (b) Characteristics of F_c versus R/X ((Delta = 0, 0.25, 0.5, 1).

4. Proposed power decoupling trajectory

This section is intended to break the linkage of Q and $\Delta\delta$ such that ΔQ is minimized. The idea is illustrated in Fig. 8. Instead of traveling on the outer circle, the initial operating point A (P_1, Q_1) is forced to move inside the circle towards B' (P_2, Q_1) on the inner circle. Eventually, ΔQ can be reduced during the transient power change. This indicates that a voltage compensation must be made to remedy the effect of $\Delta\delta$. As $\Delta\delta$ reduces, the radius of the power circle has to be adjusted accordingly to weaken the link of the reactive power and the power angle. An analysis is carried out to verify the reactive power dynamic process after the voltage compensation is added.

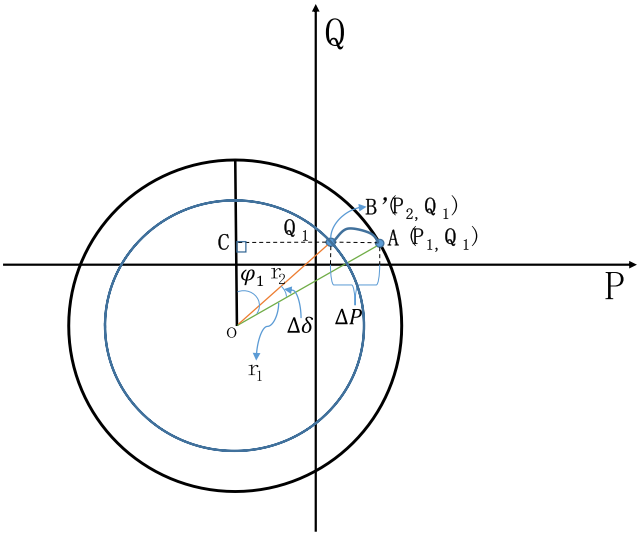

Fig. 8. Decoupling of ΔQ and $\Delta\delta$.

4.1. Power decoupling

In the triangle OB'A as shown in Fig. 8,

$$\frac{\Delta P}{\sin(\Delta\delta)} = \frac{r_2}{\sin\left(\frac{\pi}{2} - \varphi_1\right)} = \frac{r_2}{\cos(\varphi_1)} \tag{10}$$

where, r_2 is the radius of the inner circle. When,

$$\varphi_1 = \delta_1 + \tan^{-1}(R/X) \tag{11}$$

Hence,

$$\Delta P = r_2 \sin\Delta\delta/\cos\varphi_1 \tag{12}$$

Define

$$A_\delta = r_2/\cos\varphi_1 \tag{13}$$

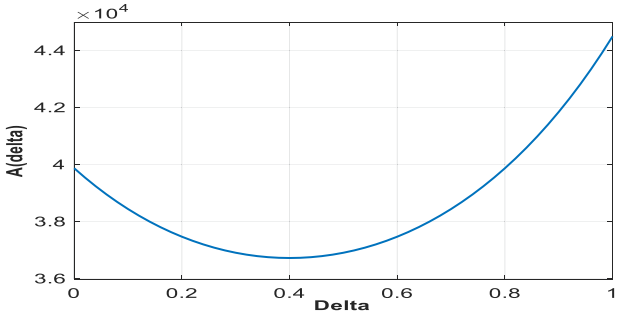

Fig. 9. A_δ variation versus $\Delta\delta$.

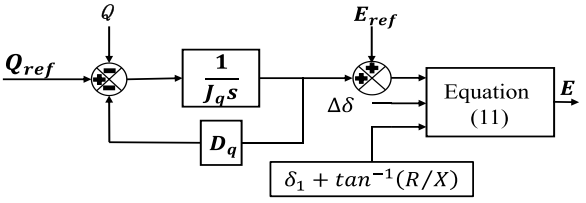

Fig. 10. Voltage compensation scheme.

Then

$$\Delta P = A_\delta \sin \Delta\delta \tag{14}$$

The relationship between the outer circle radius r_1 and r_2 is represented by:

$$r_1 / \sin\left(\frac{\pi}{2} + \varphi_1 - \Delta\delta\right) = r_2 / \sin\left(\frac{\pi}{2} - \varphi_1\right) \tag{15}$$

This leads to

$$r_2 = r_1 \cos\varphi_1 / \cos(\varphi_1 - \Delta\delta) \tag{16}$$

Since the radius r is proportional to the VSG output voltage E, in response to the change of $\Delta\delta$, a voltage compensation E_2 corresponding to r_2 is obtained as below,

$$E_2 = E_1 \cos\varphi_1 / \cos(\varphi_1 - \Delta\delta) \tag{17}$$

A_δ is also a function of r_1 and $\Delta\delta$ that can be expressed as (18) and shown as Fig. 9.

$$A_\delta = r_1 / cos(\varphi_1 - \Delta\delta) \tag{18}$$

Therefore, the voltage compensation scheme is shown as Fig. 10.

4.2. Stable P control-loop

The active power P delivered to the PCC is expressed as:

$$P = \Delta P + P_1 = A_\delta \sin \Delta\delta + P_1 \tag{19}$$

If $\Delta\delta$ varies below $\pi/6$, then (19) becomes:

$$P = A_\delta \Delta\delta + P_1 \tag{20}$$

The swing equation is written below:

$$J\omega_m \cdot \frac{d\omega_m}{dt} = P_{in} - P + D(\omega_g - \omega_m) \tag{21}$$

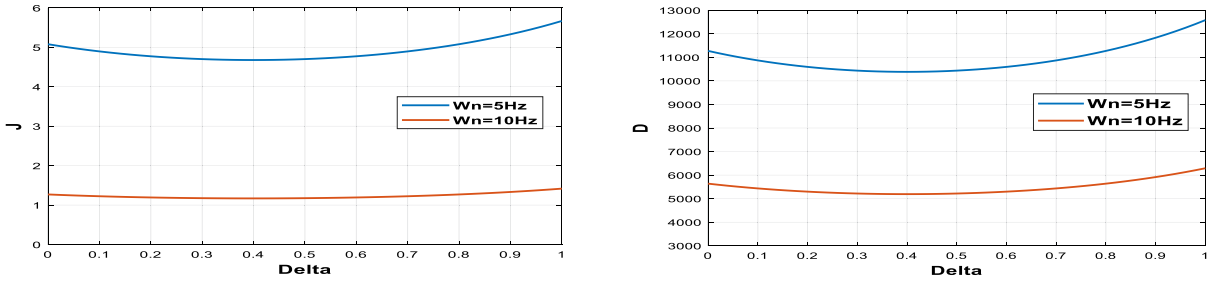

(a) (b)

Fig. 11. (a) J and (b) D variations against $\Delta\delta$.

Given that

$$\Delta\delta = \int \left(\omega_m - \omega_g\right) dt \tag{22}$$

Then,

$$\omega_g = 2\pi f_0 \tag{23}$$

The derivative of (19) is

$$dP/dt = A_\delta(\omega_m - \omega_g) \tag{24}$$

The 2nd order derivative is derived

$$d^2P/dt^2 = A_\delta d\omega_m/dt \tag{25}$$

Plug (24) and (25) into (23), a second order differential equation is obtained in terms of P:

$$\frac{J\omega_m}{A_\delta} \cdot \frac{d^2P}{dt^2} + \frac{D}{A_\delta} \cdot \frac{dP}{dt} + P = P_{in} \tag{26}$$

where $J\omega_m$ is a coefficient that varies together with ω_m. J and D curves are shown as Fig. 11. Apply Laplace transformation to (26), the transfer function between P and P_{in} is derived:

$$\frac{P(s)}{P_{in}(s)} = \frac{A_\delta/J\omega_m}{s^2 + (D/J_\omega)s + A_\delta/J\omega_m} \tag{27}$$

Compared to the standard form of the second order equation, the natural frequency ω_n and damping factor ζ are found as below:

$$\omega_n = \sqrt{A_\delta/J\omega_m} \tag{28}$$

$$\zeta = D/2\sqrt{A_\delta/J\omega_m} \tag{29}$$

4.3. Active and reactive power regulation for LVRT

The distributed generations based on VSG are normally connected to the medium and low voltage distribution network. And the short-circuit is the most possible fault in the distribution network. When a short-circuit fault occurs in the power grid, the traditional distributed generations are usually switched off from the power grid to avoid the overcurrent. Although it can protect the distributed generations, too many disconnections will exacerbate the grid failure. In order to protect the safety of the power grid and improve the utilization efficiency of distributed generations, the distributed generations are required to continue to operate while the voltage of PCC sags. At the same time, a certain amount of reactive power is required to inject to the power grid to support the grid voltage. And the active power also needs to be reduced to prevent overcurrent during the grid fault. When the power grid fault is over, both reactive power and active power can restore to be the original value [11–13].

Due to the voltage of PCC sags, the active power will decrease as shown in Fig. 12(a). According to EAC, the system will be unstable if the maximum deceleration area is smaller than the acceleration area. Therefore, the reference of active power is designed to be adjusted as shown in Fig. 12(b). Because the active power and reactive power play an important role in the control during the grid fault, the dynamic power decoupling is sensitive for the transient response of LVRT [14,15]. Where P_{ref} is the original reference and $P_{\text{ref}*}$ is the updated reference of the

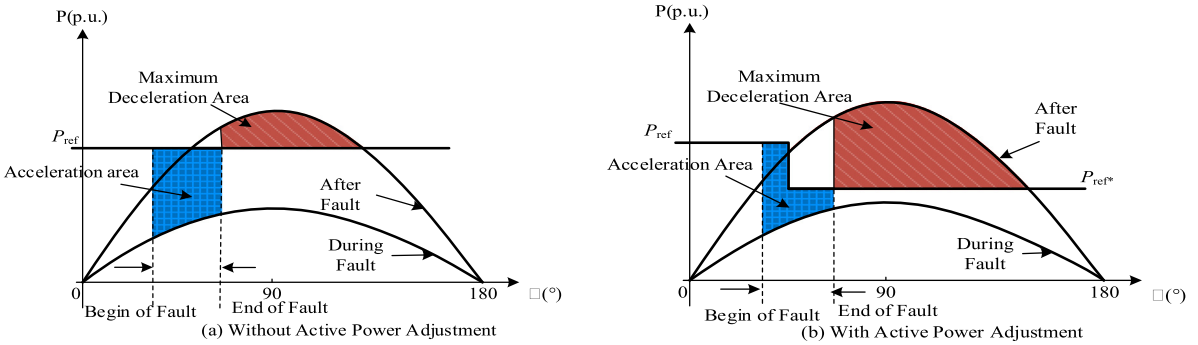

Fig. 12. P_{ref} curve for LVRT.

active power.

5. Simulation and experiment results

5.1. Simulation

In order to verify the effectiveness of the algorithm, a simulation model was built in MATLAB. The parameters of the model are shown in Table 1. To create a large-signal span of the power angle, the active-power took a big step-down. The original P is set to 1650 W and Q is 0 Var. At 0.1 s, the working load is switched down to 700 W in Fig. 13 where Q in (a), without decoupling, is around 200 Var and Q in (b) is reduced to 50 Var after compensation during the transients. Contrarily to Fig. 13(a), the transition time in Fig. 13(b) is halved from 0.2 s to 0.1 s after the voltage compensation discussed in Section 4 was implemented. Therefore, the dynamic performance has been enhanced together with the proposed algorithm.

Table 1. Parameters of the simulation model.

Parameters	Value	Parameters	Value
Rated frequency	50 Hz	DC voltage	800 V
Switching frequency	10 kHz	Inductance of line	4 mH
Rated AC voltage	380 V	Capacitor of filter	10 μF
Resistance of line	0.4 Ω	Filter inductor	2 mH
Virtual moment of inertia	40	Damping factor	0.05

As shown in Figs. 14 and 15, it is the waveform of LVRT for the single-phase fault under grid-on mode. The single-phase voltage drops to 50% of the rated voltage. The active power decreases to restrain the current and the reactive power increases to support the voltage of power grid during the fault. When the single-phase fault is over, the active power and reactive power restore to be the normal value. The dynamic characters have been improved by graphical decoupling compared with no compensation mode.

5.2. Experiment

An experimental platform was set up to test the control strategy as shown in Fig. 16. The VSG operated with a working load of 1.5 kW initially. Then, the 1 kW working load would be switched off to test the algorithm.

Figs. 17 and 18 record the experimental waveforms of P, Q and three-phase currents of the VSC during the step-down of P. Comparisons have been made before and after the proposed decoupling compensation was incorporated.

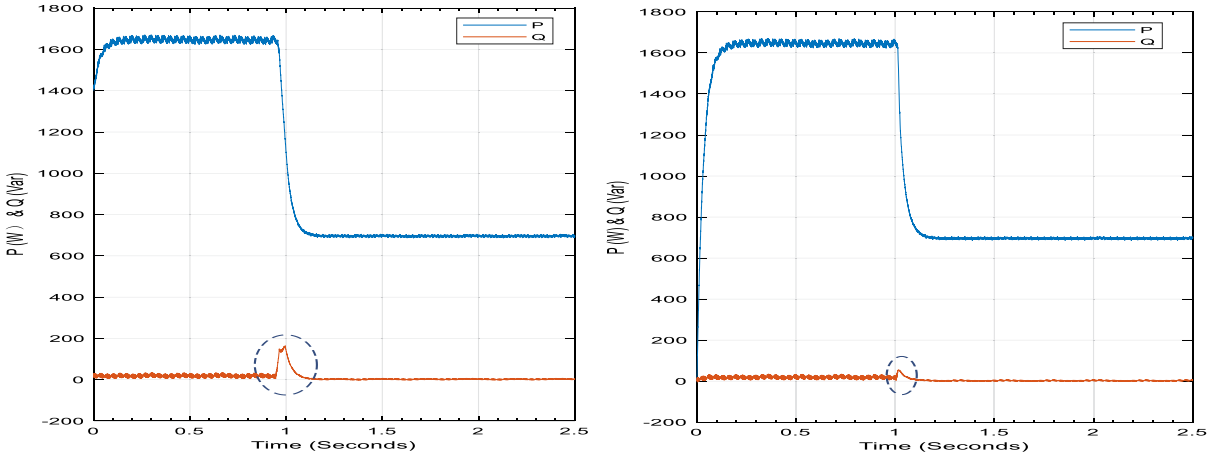

(a) Without compensation (b) With decoupling

Fig. 13. The step-down operation of P & coupled Q waveforms under islanding mode.

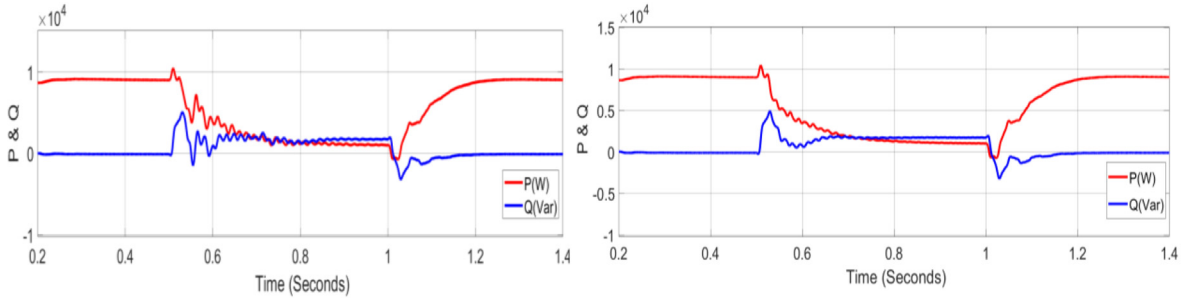

(a) LVRT Without compensation (b) LVRT With decoupling

Fig. 14. LVRT of P & Q under grid-on mode.

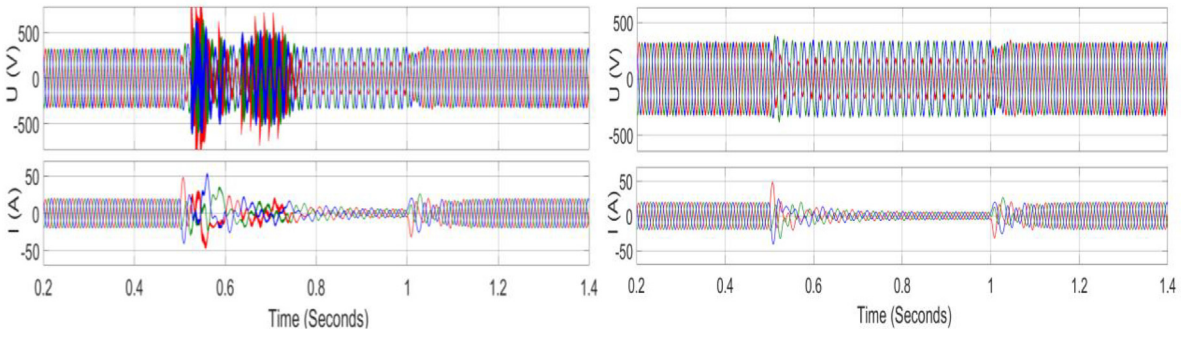

(a) LVRT Without compensation (b) LVRT With decoupling

Fig. 15. LVRT of U & I under grid-on mode.

It is found that the measured Q in Fig. 17(a) has been reduced from 150 Var to 50 Var shown in Fig. 17(b) during the transients. In addition, the transition time in Fig. 17(a) is measured to be 0.012 s while the transient time in Fig. 17(b) is only about 0.005 s. The influence on the three-phase is less compared to previous case. Hence, the transient behavior with the proposed algorithm is proved to be better than that without decoupling method.

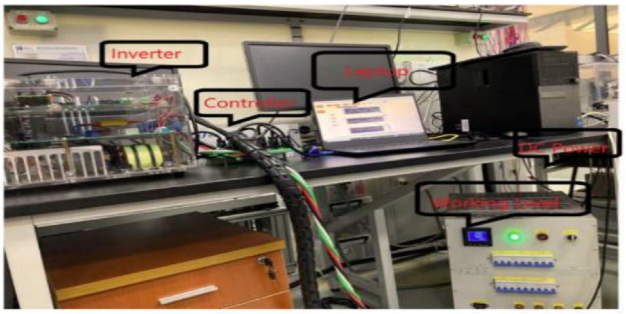

Fig. 16. The experiment platform.

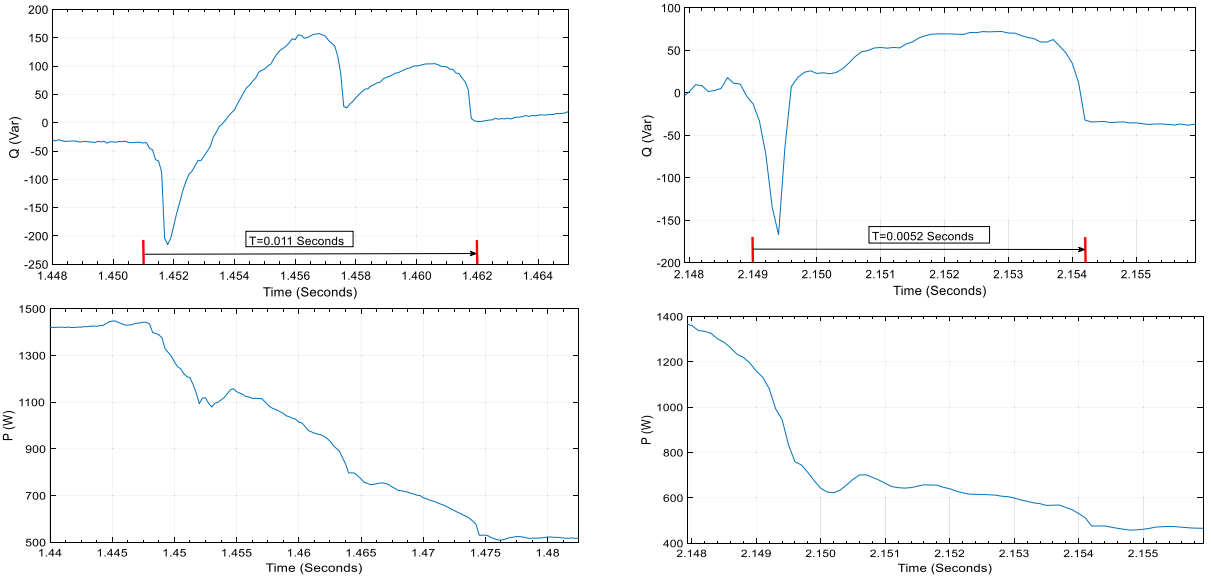

(a) Without compensation (b)With decoupling

Fig. 17. The step-down operation of P & coupled Q waveforms.

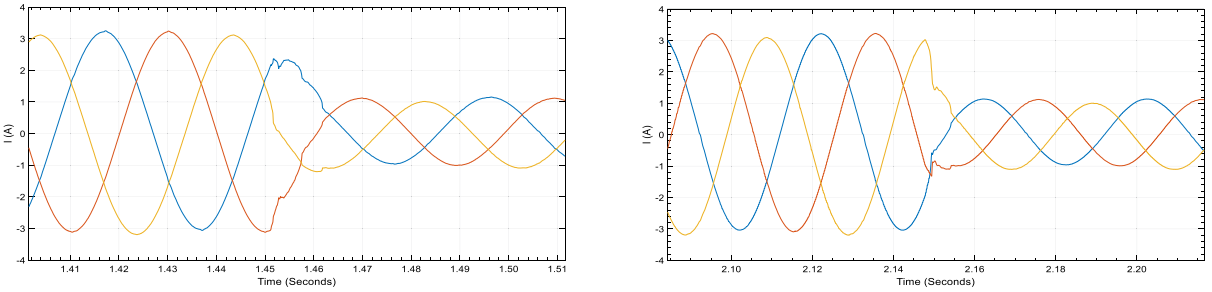

(a) Without compensation (b)With decoupling

Fig. 18. The three-phase currents of the VSC during the step-down operation of P.

6. Conclusion

A graphical model has been presented to deal with the grid-forming VSG under the large-signal angle disturbance. On the basis of the proposed model, an analysis of the transient power transfer, power decoupling and stable

operation of the P control loop have been carried out. The simulation model based on Matlab is built to verify the effectiveness of the algorithm. The simulation results show that the dynamic character can be improved for LVRT under power grid faults. An experimental platform is built to test the proposed control strategy. Compared with the traditional method, the dynamic performance of the VSG under LVRT mode has been verified to be improved.

In this project, only a single distributed generator is considered in the case. Therefore, multi-distributed generators will be taken into consideration for the future work. And the active power reference is designed to be decreased to restrain the fault current during LVRT. The more accuracy and effective control strategy of LVRT are supposed to carried out for the future research.

Declaration of competing interest

The authors declare that they have no known competing financial interests or personal relationships that could have appeared to influence the work reported in this paper.

Data availability

No data was used for the research described in the article.

Acknowledgment

This work was supported by the Ningbo Science Foundation of China (Grant no. 202003N4182).

References

[1] Harnefors L, Schweizer M, Kukkola J, Routimo M, Hinkkanen M, Wang X. Generic PLL-based grid-forming control. IEEE Trans Power Electron 2022;37(2):1201–4.
[2] Fu X, et al. Large-signal stability of grid-forming and grid-following controls in voltage source converter: A comparative study. IEEE Trans Power Electron 2021;36(7):7832–40.
[3] Chen M, Zhou D, Blaabjerg F. Enhanced transient angle stability control of grid-forming converter based on virtual synchronous generator. IEEE Trans Ind Electron 2021. http://dx.doi.org/10.1109/TIE.2021.3114723.
[4] Wen T, Zhu D, Zou X, Jiang B, Peng L, Kang Y. Power coupling mechanism analysis and improved decoupling control for virtual synchronous generator. IEEE Trans Power Electron 2021;36(3):3028–41.
[5] Li M, et al. Unified modeling and analysis of dynamic power coupling for grid-forming converters. IEEE Trans Power Electron 2022;37(2):2321–37.
[6] Nithya C, Roselyn JP. Multimode inverter control strategy for LVRT and HVRT capability enhancement in grid connected solar PV system. IEEE Access 2022;10(2022):54899–911. http://dx.doi.org/10.1109/ACCESS.2022.3175872.
[7] Shafiullah M, Ahmed SD, Al-Sulaiman FA. Grid integration challenges and solution strategies for solar PV systems: A review. IEEE Access 2022;10(2022):52233–57. http://dx.doi.org/10.1109/ACCESS.2022.3174555.
[8] Li H, Gao Z, Ji S, Ma Y, Wang F. An inrush current limiting method for grid-connected converters considering grid voltage disturbances. IEEE J Emerg Sel Top Power Electron 2022;10(2):2608–18. http://dx.doi.org/10.1109/JESTPE.2022.3147515.
[9] Jain S, Easley M, Shadm MB, Mirafzal B. Decoupled active and reactive power predictive control of impedance source microinverter with LVRT capability. In: 2018 IEEE Power and Energy Conference at Illinois (PECI). 2018, p. 1–6. http://dx.doi.org/10.1109/PECI.2018.8334982.
[10] Choopani M, Hosseinian SH, Vahidi B. New transient stability and LVRT improvement of multi-VSG grids using the frequency of the center of inertia. IEEE Trans Power Syst 2020;35(1):527–38. http://dx.doi.org/10.1109/TPWRS.2019.2928319.
[11] Fang H, Zhang X. Improvement of low-voltage ride-through capability for wave energy conversion system. IEEE Trans Ind Electron 2022;69(8):8123–33. http://dx.doi.org/10.1109/TIE.2021.3109536.
[12] Nasiri M, Arzani A, Guerrero JM. LVRT operation enhancement of single-stage photovoltaic power plants: An analytical approach. IEEE Trans Smart Grid 2022;12(6):5020–9. http://dx.doi.org/10.1109/TSG.2021.3108391.
[13] Chen S, Yao J, Liu Y, Pei J, Huang S, Chen Z. Coupling mechanism analysis and transient stability assessment for multiparalleled wind farms during LVRT. IEEE Trans Sustain Energy 2022;12(4):2132–45. http://dx.doi.org/10.1109/TSTE.2021.3083830.
[14] Hasan S, Agarwal V. An unconstrained voltage support scheme for distributed generation connected to resistive-inductive grid under unbalanced conditions. IEEE Trans Ind Appl 2022;57(4):4253–62. http://dx.doi.org/10.1109/TIA.2021.3079383.
[15] Khan MA, Haque A, Kurukuru VSB. Dynamic voltage support for low-voltage ride-through operation in single-phase grid-connected photovoltaic systems. IEEE Trans Power Electron 2022;36(10):12102–11. http://dx.doi.org/10.1109/TPEL.2021.3073589.